nature physics

Supplementary information

https://doi.org/10.1038/s41567-026-03375-4

Visualization of the Zhang–Rice singlet, electronic molecules and Cooper pair formation in a cuprate superconductor

In the format provided by the authors and unedited

This PDF files includes:

Supplementary Text

I. Schematic of electronic molecules and similarity to real molecules

The spatial distributions of electronic states for a few coupled dopants in CCOC exhibit the rod-shaped pattern consisting of short stripes at low energy and dense ladder rungs at high energy. Figure S1 displays the schematic diagrams of the two types of DOS distributions. At low energy, the overall rod-shaped patterns are spontaneously segregated into plaquettes with an average size of $4a_0$, and the internal stripes are aligned parallel with average distance around $1.2a_0$. At high energy, the ladder rungs are perpendicular to the stripes on the left with an average width around $4a_0$ and average distance close to a_0. These schematics reproduce the main experimental features and explain the Fourier transforms very well. Both the shape and orthogonality of the spatial patterns are reminiscent of molecular orbitals in real molecules, thus we dub this pattern electronic molecules.

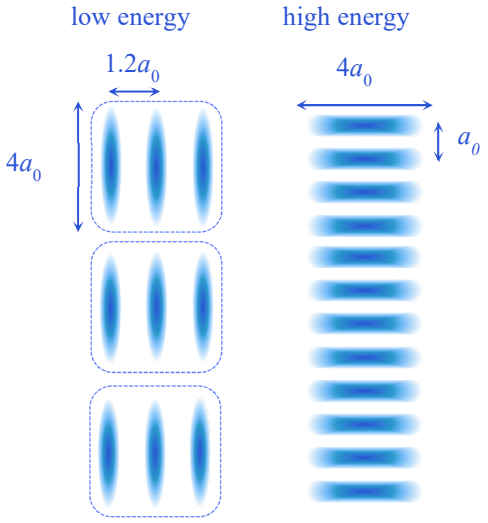

Fig. S1. Schematic diagrams of the spatial distribution of electronic states for rod-shaped electronic molecules in CCOC. The low- and high-energy DOS maps exhibit the stripe- and ladder-shaped patterns that are orthogonal to each other.

For comparisons with the experimental observations in this work, we display some typical molecular electronic state patterns observed by STM, including graphene nanoribbon (Fig. S2a)[1], triply fused porphyrin-graphene nanoribbon (Fig. S2b)[2], phenazine–gold–phenazine complex (Fig. S2c)[3] and pentacene (Fig. S2d)[4]. The molecular orbital patterns are constructed by the linear combination of different atomic orbitals with different relative phases, and the stripe and ladder shapes are quite common. Shown in Fig. S2e is an example of artificial atomic chain constructed by Cs atoms on InSb surface[5], exhibiting the orbital patterns with stripe and ladder shapes for different energies. Due to the orthogonality of wavefunctions, the local DOS maps of orbitals at different energies will be complementary to each other in the real space. Some molecules also exhibit the segregation into plaquettes or clusters.

In our experiments, we observe rod-shaped dI/dV maps for diluted holes doped into the AF insulator. The overall spatial pattern and the orthogonality between low- and high-energy electronic states are highly reminiscent of the molecular orbitals shown above. Moreover, they

originate from the overlap of Zhang-Rice singlet states, or linear combination of atomic orbitals. Therefore, the electronic states of the coupled holes can be naturally described as electronic molecules in a doped AF Mott insulator, which provide a valid basis for understanding the pairing mechanism in cuprates.

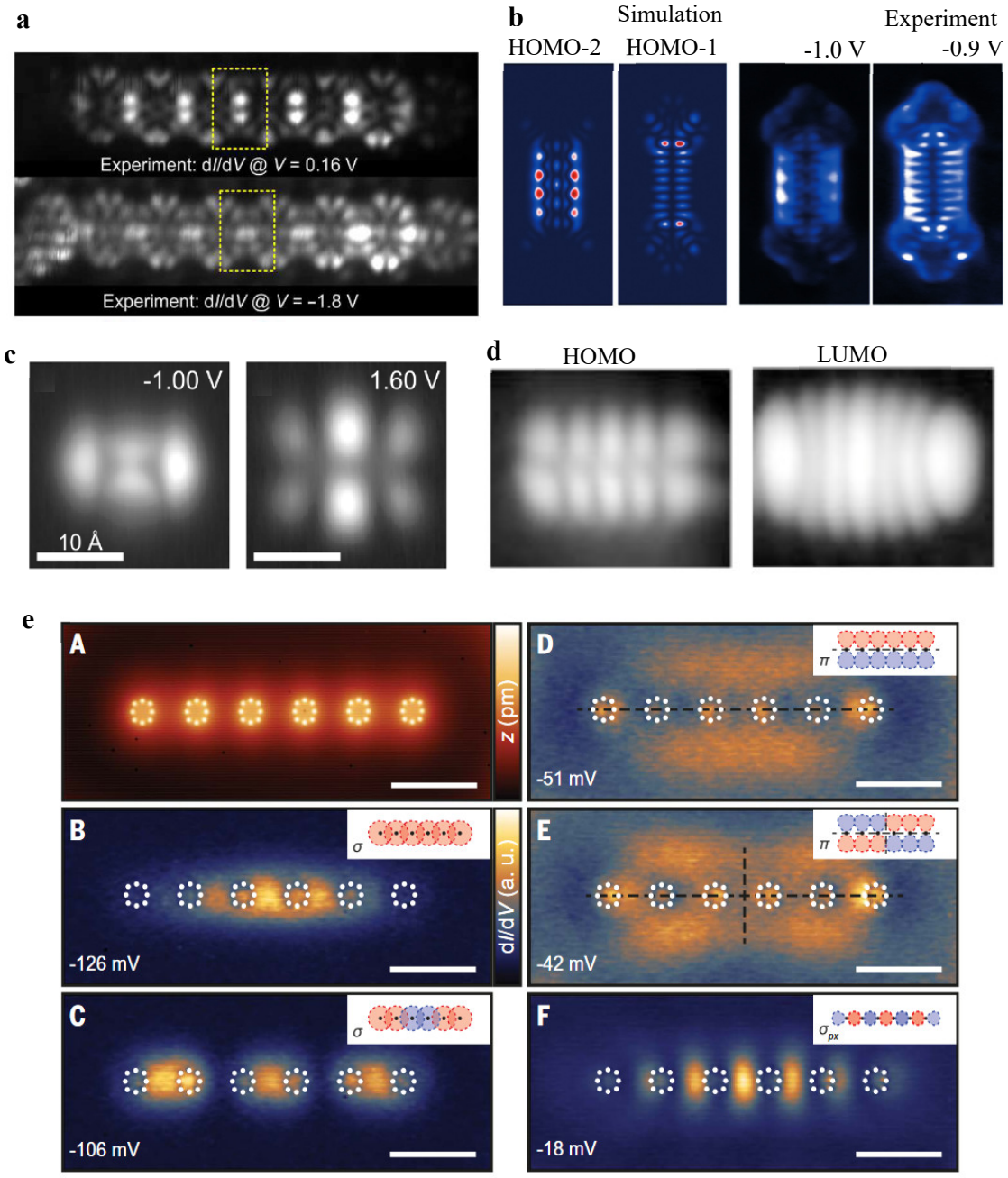

Fig. S2. The molecular orbitals of four real molecules. The d*I*/d*V* maps at representative energies in **a,** coronene-cyclobutadienoid graphene nanoribbon, adapted from Ref. 1; **b,** triply fused porphyrin-graphene nanoribbon, adapted from Ref. 2; **c,** phenazine-gold-phenazine complex, adapted from Ref. 3; and **d,** pentacene, adapted from Ref. 4. **e,** The d*I*/d*V* maps of the molecular orbitals of an artificial atomic chain, adapted from Ref. 5.

II. Similar electronic molecule physics in lightly doped $Bi_2Sr_2CuO_{6+\delta}$

To investigate the universality of the electronic molecule physics observed in this work, we studied a highly insulating $Bi_2Sr_2CuO_{6+\delta}$ (Bi-2201) with hole doping level $p = 0.05$. The Bi-2201 used here has La substitution of Sr to reduce the hole density, thus has different crystal structure and different types of dopants compared to CCOC. Nevertheless, we observe strikingly similar local electronic states, especially the clover-shaped ZRS state and stripe-ladder shaped molecular orbitals. Figure S3a displays the topographic image of the Bi-2201 taken at $T = 5$ K, clearly resolving the atomic scale crystal structure with the structural supermodulation. Figure S3b shows the dI/dV map at $V_b = 300$ mV in the FOV of Fig. S3a, which reveals three four-lobe clover patterns. Figures S3c-d are the zoom-in maps of the red box in Fig. S3b, focusing on one clover. The crosses label the Cu sites and the clover pattern shows nearly the same size and spatial distribution as the single hole state in CCOC. The spectra taken along the arrow and at the lobes/center of the clover are displayed in Fig. S3e-f, respectively. The positive bias dI/dV is enhanced on the lobes, corresponding to the increasing hole density.

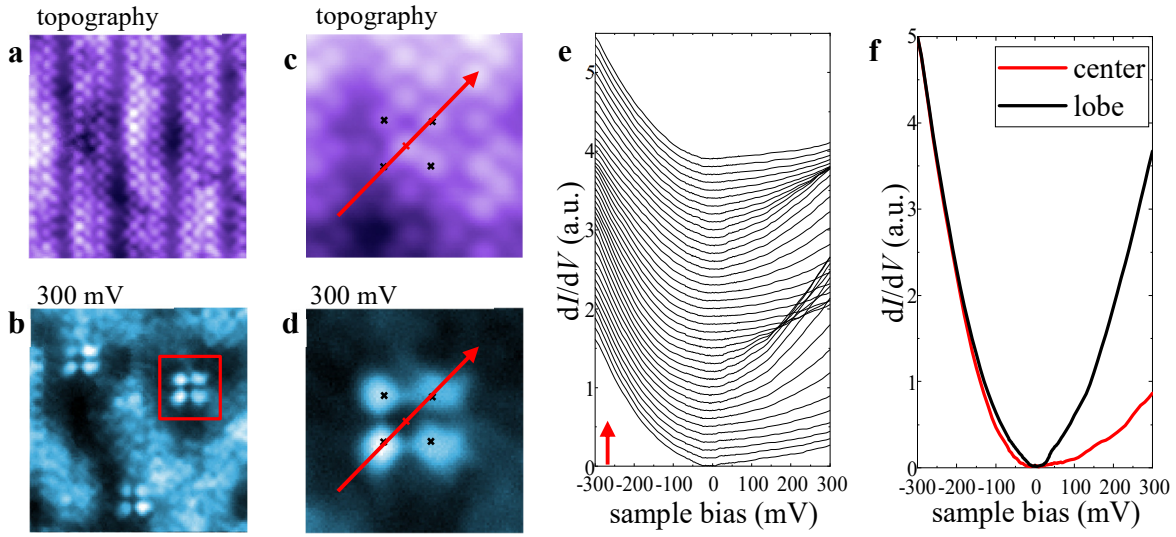

Fig. S3. The four-lobe clover pattern in underdoped Bi-2201. a, The topography of a strongly underdoped Bi-2201 with $p = 0.05$. **b**, The dI/dV map at 300 mV in the area of **a**. **c-d**, The zoom-in maps of a clover pattern enclosed by the red box in **b**. **e**, The dI/dV spectra taken along the arrow in **c-d**. **f**, The spectra taken at the lobes and center of the clover, as marked by the crosses with corresponding colors in **c** and **d**.

In Figures S4a and S4b, we present dI/dV maps at $V_b = 50$ mV and 300 mV in a larger FOV. Here, stripe- and ladder-shaped molecular orbitals are observed at low and high energies, respectively, strikingly similar to that in CCOC. The periodicity of the molecular orbitals in Bi-2201 appears less regular than in CCOC, most likely due to the structural distortion of the CuO_2 planes caused by the supermodulation. Additionally, the presence of various types of

dopants in the Bi-family cuprate may contribute to the complexity of molecular orbital formation. The low-energy gaps are also present on the stripe-shaped molecular orbital pattern. Figures S4c-d display the U-shaped and V-shaped gap along the linecut in Fig. S4a, respectively. The co-existence of the U-shaped and V-shaped gap is also the same as that in CCOC, further demonstrating the universality of electronic molecule physics in cuprates.

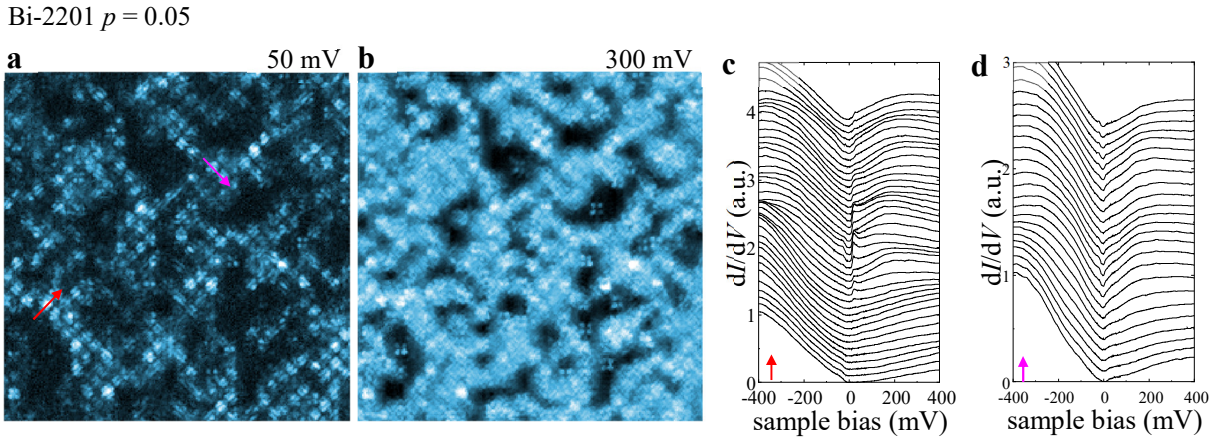

Fig. S4. The electronic molecule features and the low-energy gaps in Bi-2201. a-b, The dI/dV maps at 50 mV and 300 mV in the underdoped Bi-2201 sample. **c-d**, The spectra taken along the arrows in **a** with corresponding colors, showing the predominant U- and V-shaped gaps, respectively.

III. Estimation of the plaquette density in the p = 0.10 sample

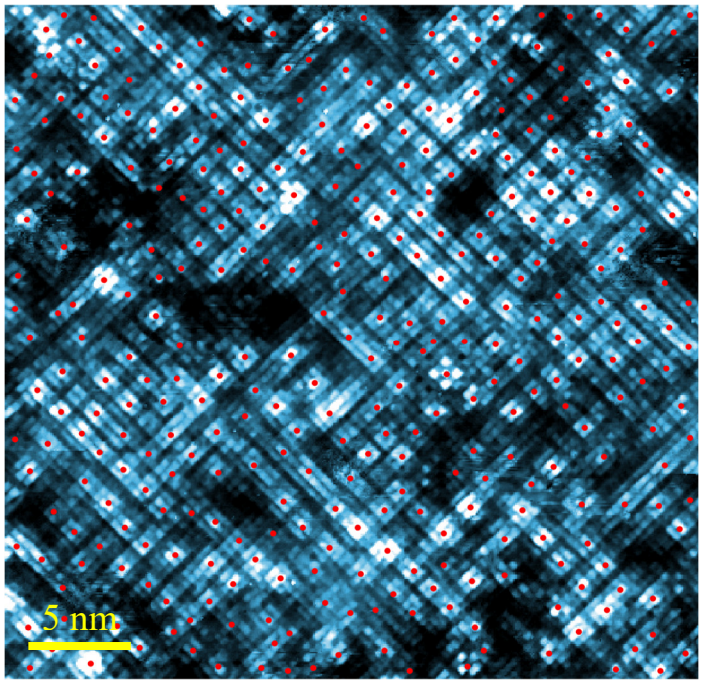

Fig. S5. Estimation of the plaquette density. Current map of the p = 0.10 sample at 30 mV. The red dots indicate the positions of plaquette centers.

In Bi-2201, it has been demonstrated that each checkerboard plaquette hosts ~2 holes, which may correspond to a local Cooper pair[6]. The checkerboard plaquette thus serves as the fundamental unit for pairing. Employing the same method, we estimate the density of checkerboard plaquettes in the p = 0.10 CCOC sample, as depicted in Fig. S5. The detailed methodology is outlined in Ref. 6. The calculated plaquette density is approximately $0.048/a_0^2$. Given the p = 0.10 hole density, each plaquette thus hosts 0.10/0.048 ~ 2.07 holes. The observation is consistent with that in Ref. 6 for Bi-2201, while the absence of structural supermodulation and much simpler dopants in CCOC make the conclusion more compelling. This finding significantly strengthens the conclusion that the electronic molecules play a pivotal role in the pairing mechanism of high-T_c superconductivity.

IV. Energy and spatial evolutions of the single hole state in p = 0.03 sample

With increasing hole density in CCOC above p = 0.03, the isolated single hole with symmetric electronic state centered around the dopant disappear. The reason is that the electronic potential fluctuation of other dopants is always strong enough to break the degeneracy of the four nearest neighboring Cu sites. The energy dependence of the single hole electronic state in the p = 0.03 sample is displayed in Fig. S6. With increasing energy, the four-lobe clover pattern emerges gradually from the dark background, as shown in Fig. S6d-e.

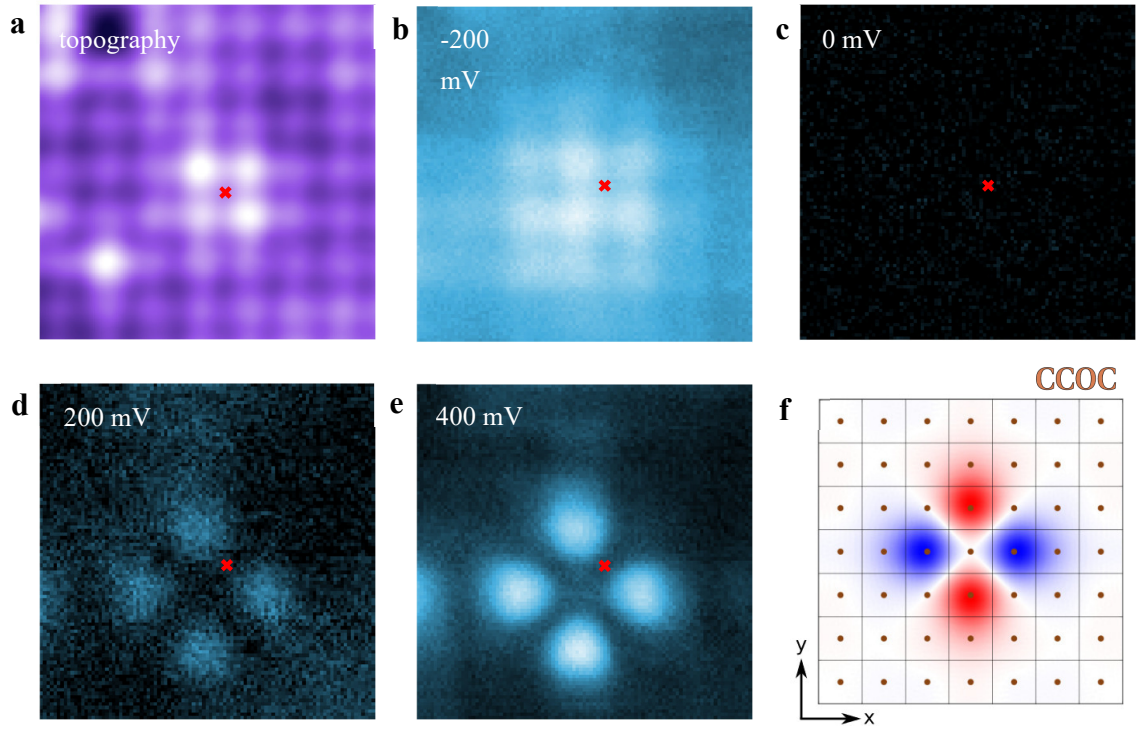

Fig. S6. Spatial distribution of the single hole state at different biases. a, The topography of a single dopant in the p = 0.03 sample. **b-e,** The dI/dV maps at bias voltage V_b = -200, 0, 200, and 400 mV, respectively. The electronic state closest to the E_F at positive bias shows the four-lobe clover pattern. **f**, The Wannier function of CCOC, as a color map approximately 5 Å above the surface exposed to the STM tip, adapted from Ref. [7].

The dopant is Ca-centered while the electronic state is Cu-centered. The mismatch between the center of electronic state and the dopant position demonstrates that the doped hole is loosely bounded to the dopant by Coulomb attraction, but the dopant potential does not directly participate in the formation of electronic state. The observed single hole state reflects the fundamental nature of a doped hole in the CuO_2 plane, which is the predicted Zhang-Rice singlet state. The observed four-lobe shape is also similar to the calculated Wannier function in the cuprate[7], as shown in Fig. S6f, further demonstrating that it is the fundamental single hole electronic state.

V. The setpoint parameters for the STM measurements

The setpoint effect refers to the mismatch between the measured differential conductance dI/dV and the intrinsic electronic density of states (DOS) of the sample. The local dI/dV at a given energy is proportional to the sample DOS at the corresponding bias voltage divided by the integrated DOS from zero to the setup bias voltage. The deviation of the measured dI/dV map from the intrinsic DOS map is particularly severe under two conditions: (1) when the local DOS in the numerator is comparable to the integrated DOS in the denominator; (2) when there is strong spatial DOS modulation at other energies than that of interest.

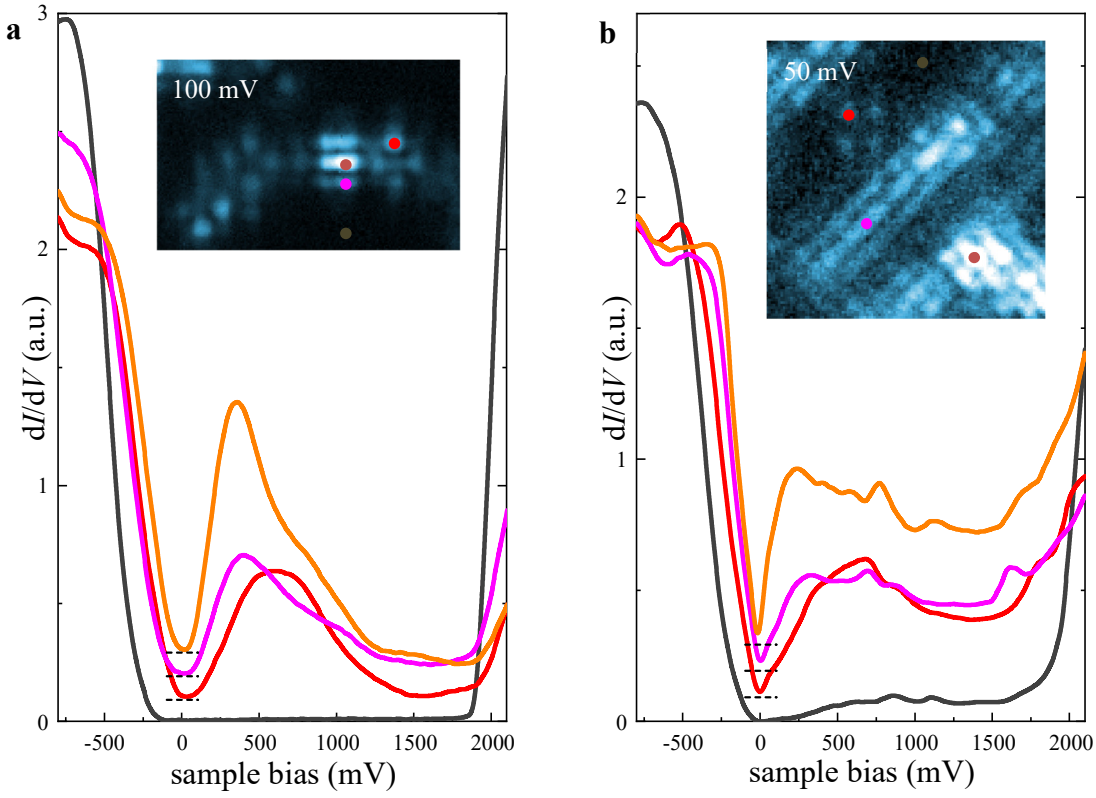

Fig. S7| a, Large energy range spectra measured at dot-marked positions in the dI/dV map at V_b = 100 mV in the inset acquired in a p = 0.03 sample. **b**, Similar dataset on the p = 0.05 sample.

To mitigate the influence of setpoint, we consistently use a large negative setup bias voltage when doing STM experiments on underdoped CCOC. Due to the well-known tunneling

asymmetry in cuprates[8], as well as directly shown by our own data (Fig. S7), the dI/dV value increases steeply at negative bias starting from around -250 mV. With a large negative setup bias voltage, the DOS at low energy is only a tiny fraction of the integrated DOS in the denominator. For example, in the most underdoped sample, we typically use a setup bias voltage around -1000 mV, whereas the stripe-plaquette features are measured at around 50 mV. In the superconducting sample, we typically use a setup bias voltage around -300 mV, while the low-energy features occur near 10-30 mV. The substantial difference ensures that low-energy dI/dV maps reliably reflect the intrinsic DOS distribution.

In addition to these arguments, we also have direct experimental evidence to validate our methodology. In Fig. S8-S10, we present dI/dV maps of a p = 0.05 insulating sample acquired at three different setpoint biases (-800 mV, -1200 mV, +2200 mV). The low-energy maps at both negative and positive biases show nearly identical spatial patterns (Fig. S8) that is insensitive to the setpoint. Moreover, this consistency extends to higher-energy features: ladder-shaped patterns in dI/dV maps (Fig. S9) remain invariant across all setup bias voltage values. At very high energy (e.g. ±400 mV, shown in Fig. S10), the dI/dV maps have no pronounced spatial modulations. The robustness of the spatial features with varied setup parameters confirms that our dI/dV measurements faithfully represent the intrinsic DOS, owing to the appropriate selection of setup conditions.

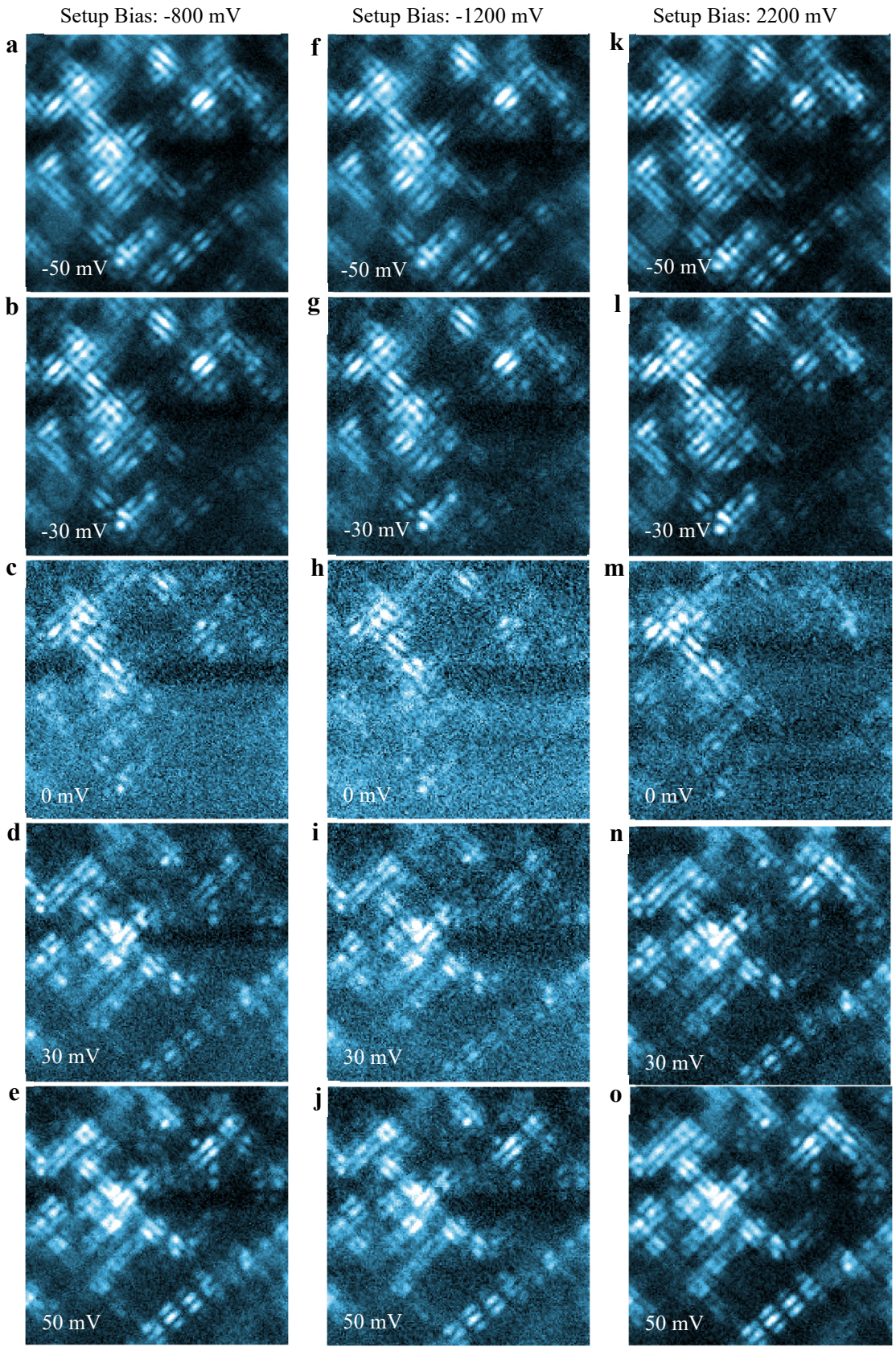

Fig. S8| a-e, The dI/dV maps on a p = 0.05 insulating sample taken at -50, -30, 0, 30, 50 mV with setup bias voltage -800 mV. **f-j**, The same dataset for setup bias voltage -1200 mV. **k-o**, The same dataset for setup bias voltage +2200 mV.

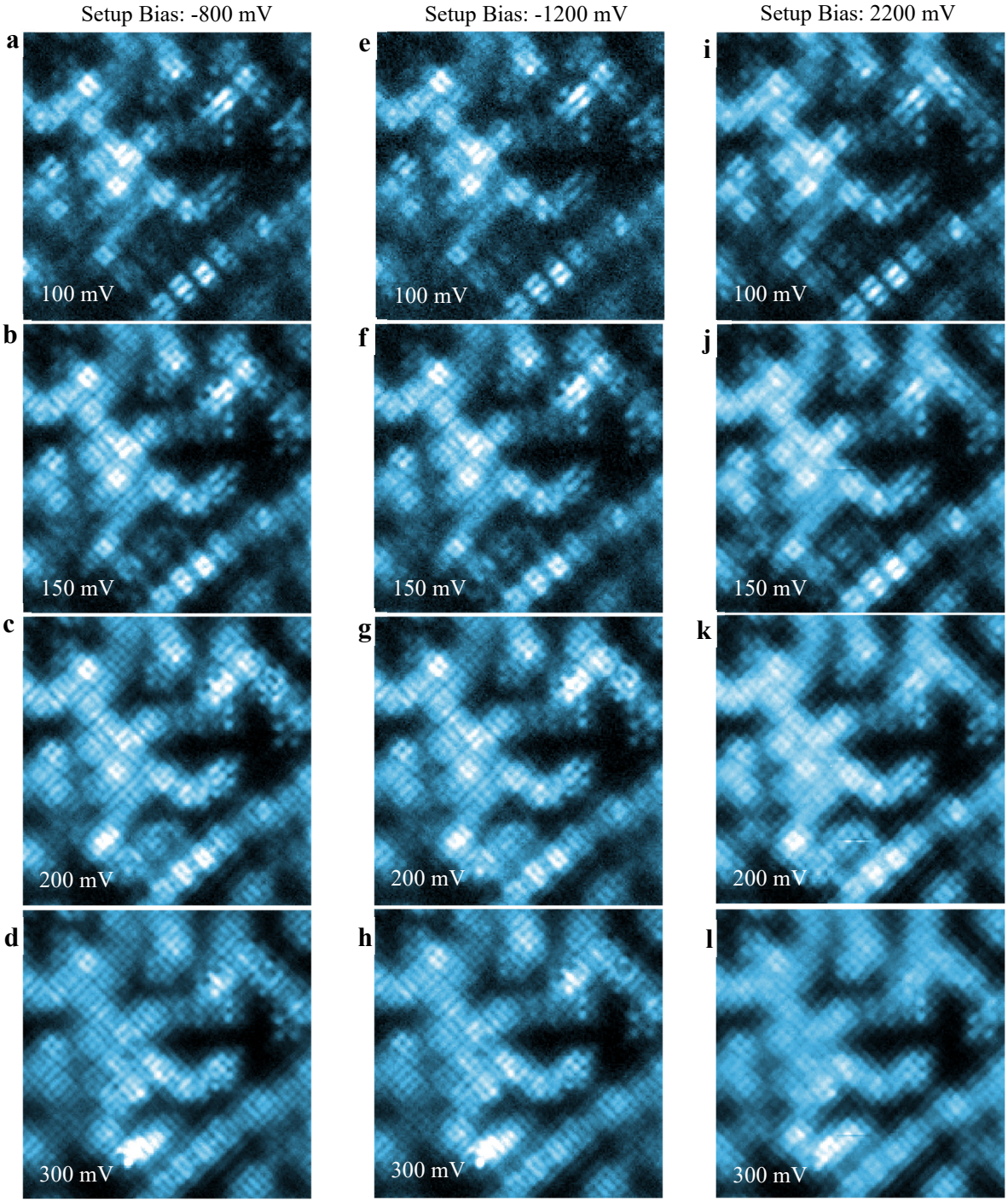

Fig. S9| a-d, The dI/dV maps on a p = 0.05 insulating sample taken at 100, 150, 200, 300 mV with setup bias voltage -800 mV. **e-h**, The same dataset for setup bias voltage -1200 mV. **i-l**, The same dataset for setup bias voltage +2200 mV.

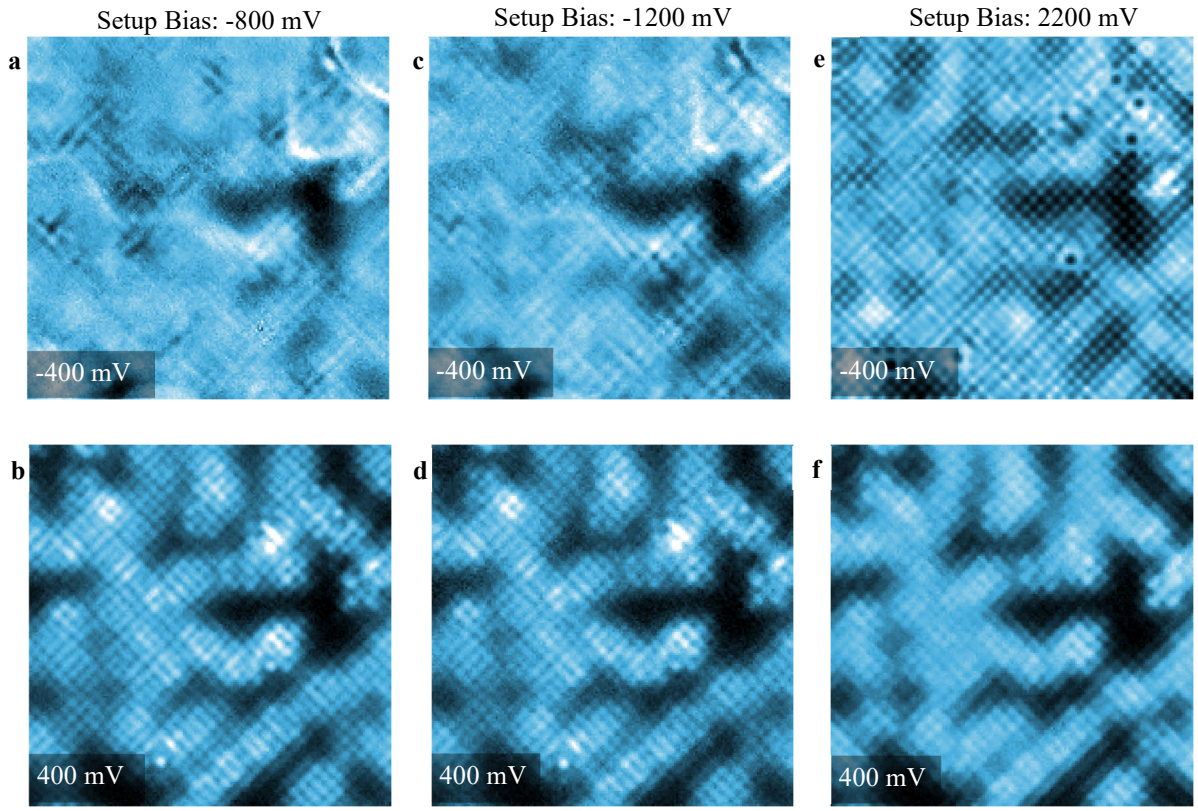

Fig. S10| a-b, The dI/dV maps on a p = 0.05 insulating sample taken at -400, 400 mV with setup bias voltage -800 mV. **c-d**, The same dataset for setup bias voltage -1200 mV. **e-f**, The same dataset for setup bias voltage +2200 mV.

In Table S1 below, we list the complete measurement parameters, including setpoint bias voltage, tunneling current, lock-in amplifier frequency, and the amplitude of modulation voltage for all measurements shown in the manuscript.

Figure	Setpoint bias (mV)	Tunneling Current (pA)	Lock-in amplifier frequency (Hz)	Amplitude of modulation voltage (mV)
Fig. 1d	-1100	102	663.137	56.6
Fig. 1f, h	-1100	102	663.137	42.4
Fig. 1j, l	-1000	104	663.137	56.6
Fig. 2a-e	-1000	176	633.137	53.0
Fig. 2h	-800	218	665.137	14.1
Fig. 2i (spectra)	-400	171	665.137	2.1
Fig. 2i (inset dI/dV map)	-800	171	665.137	53.0
Fig. 3b-c	-600	168	688.137	14.1
Fig. 3d-f	-300	168	688.137	2.1
Fig. 4a	-500	129	920.137	5.6
Fig. 4f, h	-400	180	920.137	2.1
Fig. 4g, i	-300	168	688.137	2.1
Extended Data Fig. 1	-1100	102	663.137	56.6
Extended Data Fig. 2	-1000	104	663.137	56.6
Extended Data Fig. 3	-1000	104	663.137	56.6
Extended Data Fig. 4b-d	-1000	176	633.137	53.0
Extended Data Fig. 4f-h	-800	171	665.137	53.0
Extended Data Fig. 6	-800	171	665.137	53.0
Extended Data Fig. 7b, c, f, g, j, k	-600	168	688.137	14.1
Extended Data Fig. 7d, h, l	-300	168	688.137	2.1
Extended Data Fig. 8a-c	-300	158	757.137	4.2
Extended Data Fig. 8d-e	-300	258	757.137	1.7
Extended Data Fig. 9a	-1000	176	633.137	53.0
Extended Data Fig. 9b	-600	168	688.137	14.1
Extended Data Fig. 9c	-300	158	757.137	4.2
Extended Data Fig. 9d	-500	129	920.137	5.6
Extended Data Fig. 10	-500	129	920.137	5.6
Extended Data Fig. 11a, c	-500	129	920.137	5.6
Extended Data Fig. 11g	-300	158	757.137	4.2
Extended Data Fig. 11i	-600	168	688.137	14.1
Extended Data Fig. 11k	-1000	176	633.137	53.0
Extended Data Fig. 13a	-600	168	688.137	14.1
Extended Data Fig. 13c	-300	168	688.137	2.1
Extended Data Fig. 13d	-300	158	757.137	4.2
Extended Data Fig. 13f	-300	258	757.137	1.7
Extended Data Fig. 13g	-500	129	920.137	5.6
Extended Data Fig. 13i	-400	180	920.137	2.1
Extended Data Fig. 14	-500	129	920.137	5.6
Fig. S7a-e, Fig. S8a-d, Fig. S9a-b	-800	165	643.137	14.1
Fig. S7f-j, Fig. S8e-h, Fig. S9c-d	-1200	196	643.137	14.1
Fig. S7k-o, Fig. S8i-l, Fig. S9e-f	2200	79	643.137	14.1

Table S1| The setpoint bias voltage, tunneling current, lock-in amplifier frequency and the amplitude of modulation voltage for all the measurements shown in the manuscript.

References

1. Jacobse, P. H. *et al.* Pseudo-atomic orbital behavior in graphene nanoribbons with four-membered rings. *Sci. Adv.* **7**, eabl5892 (2021).
2. Mateo, L. M. *et al.* On-surface synthesis and characterization of triply fused porphyrin–graphene nanoribbon hybrids. *Angewandte Chemie* **132**, 1350–1355 (2020).
3. Albrecht, F., Neu, M., Quest, C., Swart, I. & Repp, J. Formation and characterization of a molecule–metal–molecule bridge in real space. *J. Am. Chem. Soc.* **135**, 9200–9203 (2013).
4. Repp, J., Meyer, G., Stojković, S. M., Gourdon, A. & Joachim, C. Molecules on insulating films: scanning-tunneling microscopy imaging of individual molecular orbitals. *Phys. Rev. Lett.* **94**, 026803 (2005).
5. Sierda, E. *et al.* Quantum simulator to emulate lower-dimensional molecular structure. *Science* **380**, 1048–1052 (2023).
6. Ye, S. *et al.* The emergence of global phase coherence from local pairing in underdoped cuprates. *Nat. Phys.* **19**, 1301–1307 (2023).
7. Choubey, P., Kreisel, A., Berlijn, T., Andersen, B. M. & Hirschfeld, P. J. Universality of scanning tunneling microscopy in cuprate superconductors. *Phys. Rev. B* **96**, 174523 (2017).
8. Anderson, P. W. & Ong, N. P. Theory of asymmetric tunneling in the cuprate superconductors. *J. Phys. Chem. Solids* **67**, 1–5 (2006).